Unraveling the Combined Effects of Dielectric and Viscosity Profiles on Surface Capacitance, Electro–Osmotic Mobility and Electric Surface Conductivity

Douwe Jan Bonthuis[1] & Roland R. Netz[2]

[1]Physik Department, Technische Universität München, 85748 Garching, Germany
Current address: Rudolf Peierls Centre for Theoretical Physics, University of Oxford, Oxford OX1 3NP, United Kingdom
[2]Fachbereich Physik, Freie Universität Berlin, 14195 Berlin, Germany

► **Abstract.** We calculate the electro–osmotic mobility and surface conductivity at a solid–liquid interface from a modified Poisson–Boltzmann equation, including spatial variations of the dielectric function and the viscosity that where extracted previously from molecular dynamics simulations of aqueous interfaces. The low–dielectric region directly at the interface leads to a substantially reduced surface capacitance. At the same time, ions accumulate into a highly condensed interfacial layer, leading to the well–known saturation of the electro–osmotic mobility at large surface charge density regardless of the hydrodynamic boundary conditions. The experimentally well–established apparent excess surface conductivity follows from our model for all hydrodynamic boundary conditions without additional assumptions. Our theory fits multiple published sets of experimental data on hydrophilic and hydrophobic surfaces with striking accuracy, using the nonelectrostatic ion–surface interaction as the only fitting parameter.

1 Introduction

When immersed in water, particles typically acquire a net surface charge, which is compensated for by a cloud of counterions in solution. This surface charge usually dominates the interactions between particles in colloidal suspensions. The bare surface charge density can be measured using charge titration [1]. It is well established, however, that the bare surface charge density cannot be used directly in classical models to describe dynamic properties of colloidal suspensions, such as coagulation kinetics, electro–osmotic mobility and effective viscosity [2, 3, 4, 5]. Instead, the ions and water molecules within a few molecular diameters from the surfaces of the colloidal particles decisively affect the suspension's macroscopic kinetic behavior. A deep understanding of the relation between bare surface charge, electro–osmotic mobility and the closely related phenomenon of surface conductivity is of supreme importance in many areas of physical chemistry. For instance, electrophoresis is commonly used in modern–day biochemistry for separation of chemicals based on minute differences in surface properties [6]. Furthermore, electrokinetic driving is the method of choice to generate flow in microfluidic devices [7, 8], which are becoming ever more popular tools for biochemical analysis and clinical pathology. On a much larger scale, seismic activity in water–saturated soil produces electrokinetic signals, which are found to precede large earthquakes [9] and can be exploited for seismic imaging of the sub–surface [10]. Finally, the electrostatic and hydrodynamic properties of the colloid – water interface determine the stability of colloidal systems [11, 12], which is a crucial factor in many branches of chemical industry, such as those dealing with food, water purification, pharmaceuticals, paints, and ceramics. To comprehend and control the macroscopic behavior of each of these systems, detailed knowledge of the hydrodynamic and electrostatic properties of the interfacial molecular layers is indispensable. Despite the immense practical and fundamental interest, however, the effect of these microscopic properties on macroscopic kinetics is poorly understood.

Electrokinetic measurements in controlled environments are a particularly sensitive tool to assess the dynamic properties of interfacial layers. The basic model for an electrolyte in contact with a surface carrying an immobilized bare surface charge density σ_0 is sketched in Fig. 1 (a). Driven by a tangential electric field $E_\parallel$, counterions move along the surface, dragging water molecules along. This electro–osmotic flow profile $u_\parallel(z)$ can be used to estimate the "electrokinetically active" surface charge density σ_{ek}, using the Gouy–Chapman model and the Stokes equation with a no–slip boundary condition. At the same time, the electric conductivity of the interfacial fluid is higher than the bulk conductivity due to the presence of counterions [13, 14], to an extent that is usually expressed by the Dukhin number [15]. In conjunction with a suitable model, this surface conductivity can be used as an alternative way of estimating the surface charge density [16], leading to the con-

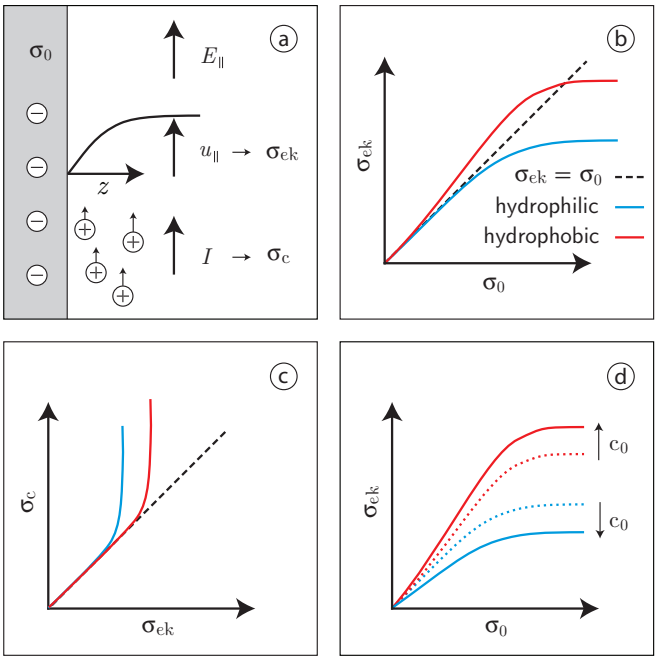

Figure 1: Sketch of the basic model and general features of experimental data. (a) An electric field $E_\parallel$ parallel to a surface with bare charge density σ_0 produces an electro–osmotic flow profile $u_\parallel(z)$, from which the electrokinetic surface charge density σ_{ek} is calculated. The conductive surface charge density σ_c is calculated from the electric current I in response to $E_\parallel$. (b) σ_{ek} is experimentally found to saturate as a function of σ_0; saturation occurs at higher values for hydrophobic surfaces than for hydrophilic surfaces. (c) σ_c is larger than σ_{ek} at all surface types. (d) When the bulk salt concentration c_0 is raised, σ_{ek} increases at hydrophobic surfaces, and decreases at hydrophilic surfaces.

ductive surface charge density σ_c. Clearly, the precise values of σ_{ek} and σ_c are highly model–dependent, and typically σ_0, σ_{ek} and σ_c do not agree. As a specific numerical example we consider silica nanochannels, where measuring the electrokinetic surface charge density using the streaming current at low salt concentration gives $\sigma_{ek} = -4$ mC/m^2 [17]. Calculating the conductive surface charge density in the same type of channels from measurements of the electric conductance, on the other hand, yields $\sigma_c = -50$ mC/m^2 [16], whereas the literature value for the bare charge density of silica, calculated from titration at pH = 8 and a bulk salt concentration of 1 mM, is even higher, $\sigma_0 = -100$ mC/m^2 [1]. This example shows that the discrepancies mentioned are not small corrections, but major effects. In particular, three puzzling, but universal experimental trends for σ_0, σ_{ek} and σ_c have impeded the advancement of colloidal science in the past. First, the electrokinetic surface charge density σ_{ek} is found to saturate as a function of the bare surface charge density σ_0, independent of surface roughness or polarity [3, 18, 19], see the sketch in Fig. 1 (b). Traditionally, this issue has been rationalized by invoking a spatially inhomogeneous viscosity profile at the interface [19]. Assuming a hydrodynamically stagnant interfacial water layer, the calculated electrokinetic surface charge density σ_{ek} is found to agree with experiments [18]. Using this model on hydrophobic interfaces, however, where the fluid is known to slip along the surface [20], the electrokinetic surface charge density exceeds the bare surface charge density, contrary to experimental evidence. Second, the conductive surface charge density σ_c is found to exceed the electrokinetic surface charge density σ_{ek} [16, 17, 21, 22, 23, 24, 25], see Fig. 1 (c). This excess surface conductivity is referred to as *anomalous surface conduction*, and is found for all systems, independent of surface composition [24, 25, 26]. Traditionally, the excess surface conductivity is rationalized by the awkward assumption that the ions in the hydrodynamically stagnant layer still conduct charge [3, 15, 24, 25, 27, 28, 29, 30], which is clearly at odds with physical intuition. Third, whereas the electrokinetic surface charge density σ_{ek} increases with increasing bulk salt concentration c_0 at hydrophobic surfaces, such as silver iodide, it decreases at hydrophilic surfaces, such as titanium oxide and iron oxide–hydroxide [3, 18], see Fig. 1 (d).

The experimental results described above cannot be explained within the classical model of a dilute solution of pointlike charges with spatially constant viscosity and dielectric constant. At high salt concentration and high surface charge density, several modifications of the classical model have been taken into account previously, primarily in the context of induced–charge electrokinetics [31]. Examples include steric interactions due to crowding of ions [32], electric–field induced viscosity increase near charged interfaces [19] and electric–field induced dielectric saturation [33]. Apart from the effects of high salt concentration and strong electric fields, however, the dielectric and viscous properties of the interfacial water layers differ from the bulk properties because of the pronounced structuring of the interfacial water. These molecular properties of interfacial water have only recently become accessible due to the advancement of molecular dynamics simulations.

In this paper, we include the variation of the dielectric function, which has been shown to work well in the description of interfacial capacitance [34], as well as the variation of the viscosity at the interface on the mean–field level. The profiles of the dielectric function and the viscosity are based on the results of molecular dynamics simulations of typical hydrophilic and hydrophobic surfaces in contact with pure water [35, 36]. Including a low–dielectric layer at the surface leads to accumulation of counterion charge close to the interface, thereby reducing the electro–osmotic flow independent of the hydrodynamic boundary conditions. The relation between counterion condensation enhancement and saturation of the electrophoretic mobility has been established earlier for branched polymeric particles of roughly spherical shape

[37]. In contrast, the surface conductivity is affected less by the ion condensation, explaining the discrepancies between the bare, conductive, and electrokinetic surface charge densities.

2 Mobility and Conductivity

We consider a charged planar surface in contact with water, having translational invariance in the x and y directions. Throughout the paper, the symbols $\parallel$ and $\perp$ refer to the directions parallel and perpendicular to the surface, respectively. The dielectric tensor, the viscosity, the electric field and the displacement field only depend on the perpendicular coordinate z.

► **Electrokinetic surface charge density.** For laminar flows, the electro–osmotic flow velocity profile $u_{\parallel}(z)$ in response to a parallel electric field $E_{\parallel}$ is calculated from the Stokes equation,

$$\nabla\eta(z)\,\nabla u_{\parallel}(z) = -\rho(z)\,E_{\parallel}, \tag{1}$$

with spatially varying viscosity $\eta(z)$ and charge density $\rho(z)$. Note that $\rho(z)$ is the ionic charge density and polarization charges do not enter the force balance, as shown earlier [38]. The hydrodynamic boundary condition of either slip or a high–viscosity layer is taken into account via the viscosity profile $\eta(z)$, which in conjunction with the condition $u_{\parallel}(0) = 0$ is designed to reproduce the flow profile at macroscopic distances from the interfaces, as will be explained later. The electro–osmotic mobility is found by integrating Eq. 1 twice using $u_{\parallel}(0) = 0$ as a boundary condition,

$$\frac{u_{\parallel}(z)}{E_{\parallel}} = -\int_0^z \frac{D_{\perp}(z')}{\eta(z')}\,\mathrm{d}z', \tag{2}$$

with $D_{\perp}(z)$ being the displacement field perpendicular to the surface, which obeys $\nabla D_{\perp}(z) = \rho(z)$. Experimentally, electro–osmotic velocity is measured far away from the interface. Assuming that the permittivity is spatially constant and equal to its bulk value ε_{bulk}, and $\eta(z) = \eta_{bulk}$ in Eq. 2, the electro–osmotic mobility is given by the Helmholtz–Smoluchowski equation,

$$\lim_{z\to\infty}\frac{u_{\parallel}(z)}{E_{\parallel}} = -\frac{\varepsilon_0\varepsilon_{bulk}}{\eta_{bulk}}\,\zeta, \tag{3}$$

with $\zeta = \int_0^{\infty}\left(D_{\perp}(z)/\varepsilon_0\varepsilon_{bulk}\right)\mathrm{d}z$ being the electrostatic potential at $z = 0$. A derivation of Eq. 3 is given in the Appendix. Because the surface potential is typically not measured directly, it is often more convenient to express ζ in terms of the equivalent surface charge density. Using the standard Poisson–Boltzmann relation between the surface potential and the surface charge density, which is valid on the mean–field level, the electro–osmotic mobility of Eq. 3 is expressed as an equivalent surface charge density, referred to as the electrokinetic surface charge density σ_{ek},

$$\sigma_{ek} = \sqrt{\frac{8c_0\varepsilon_0\varepsilon_{bulk}}{\beta}}\,\sinh\left[\frac{\beta e\,\zeta}{2}\right], \tag{4}$$

with c_0 being the bulk salt concentration. Eq. 4 is known as the Grahame equation. The ζ–potential is calculated using Eq. 3, where the electro–osmotic mobility is either measured experimentally or calculated from Eq. 2. A derivation of Eq. 4 is given in the Appendix.

► **Conductive surface charge density.** The electric conductivity close to charged surfaces is enhanced with respect to the bulk due to the presence of excess ionic charges. This surface conductivity can be conveniently measured in small channels at low salt concentration, in which case the contribution from the bulk vanishes [16]. The surface conductivity is given by the sum of a convective part, due to the electro–osmotic flow, and a conductive part, due to the electrophoretic mobility of the ions,

$$\begin{aligned}\frac{I}{E_{\parallel}} = &\int_0^{\infty} e\big[c_+(z) - c_-(z)\big]\left[u_{\parallel}(z)/E_{\parallel}\right]\mathrm{d}z \\ &+\int_0^{\infty} e\big[\nu_+\left(c_+(z) - c_0\right) + \nu_-\left(c_-(z) - c_0\right)\big]\mathrm{d}z,\end{aligned} \tag{5}$$

with $\nu_{\pm}$ being the electrophoretic mobility of the positive and negative ions. Note that we subtract the bulk contribution from the conductive part of Eq. 5. Similar to the Grahame equation (Eq. 4), the surface conductivity can be expressed as an equivalent surface charge density using the Gouy–Chapman theory, giving

$$\sigma_c = \frac{\kappa^2\eta_{bulk}}{4ec_0 + \nu\kappa^2\eta_{bulk}}\sqrt{\frac{I}{E_{\parallel}}}\sqrt{\frac{I}{E_{\parallel}} + \frac{32e^2c_0^2}{\kappa^3\eta_{bulk}} + \frac{8ec_0\nu}{\kappa}}. \tag{6}$$

A derivation of Eq. 6 is given in the Appendix. Since KCl and KNO_3 are the predominant salt types considered in the experiments that we compare our results with, we assume $\nu_+ = \nu_- = \nu$, which is a good approximation for both KCl and KNO_3.

► **Viscosity and dielectric profile.** We model the variations in viscosity at the interface by a step function,

$$\eta(z) = \begin{cases}\eta_i & \text{if } z < z_s \\ \eta_{bulk} & \text{otherwise,}\end{cases} \tag{7}$$

with η_i being the viscosity in the interfacial layer of width z_s and η_{bulk} being the bulk viscosity. The value of z_s is estimated from the flow profile calculated in molecular dynamics simulations of a shear flow between parallel plates. Note that the definition of a viscosity at sub–atomic length scales is problematic, and the profile of Eq. 7 is only intended to reproduce, within a continuum model, the flow characteristics found experimentally at distances $z > z_s$. For most hydrophobic surfaces the

fluid slips along the wall [39], which is commonly taken into account by the Navier hydrodynamic boundary condition, $b\nabla u_{\parallel}(z)|_0 = u_{\parallel}(z)|_0$, with positive slip length b. In simulations of water at a very hydrophobic diamond surface, the viscosity is found to be constant and equal to the bulk value η_{bulk} for $z > 0.15$ nm, and the slip length has a value of $b = 2.15$ nm. Setting $u_{\parallel}(0) = 0$, we reproduce the same flow profile for $z > z_s$ by assigning $\eta_i = \eta_{bulk}/15$ and $z_s = 0.15$ nm. For most hydrophilic surfaces, on the other hand, the fluid in the first molecular layer adjacent to the wall sticks to the surface [39]. Molecular dynamics simulations on smooth hydrophilic surfaces have shown that the interfacial layer is not truly stagnant, it merely has an enhanced viscosity [35, 40]. Following the simulation results of Ref. [35] we take $z_s = 0.3$ nm and $\eta_i = 3\eta_{bulk}$. In Fig. 2 (a), we show the viscosity profile $\eta(z)$ of Eq. 7 at hydrophilic and very hydrophobic surfaces. For easy reference, we characterize each viscosity profile by its apparent slip length,

$$b = z_s\left(\eta_{bulk}/\eta_i - 1\right). \tag{8}$$

Whereas a positive slip length – as is commonly found at hydrophobic surfaces – corresponds to a reduced interfacial viscosity, an enhanced interfacial viscosity – as is commonly found at hydrophilic surfaces – corresponds to a negative apparent slip length.

In general, the electrophoretic mobility of ions $\nu_{\pm}$ depends on the ion concentration and the viscosity of the fluid [41]. The ion mobility directly at the interface is not known (note that the conclusion that the interfacial mobility equals the bulk mobility [27] relies heavily on the electrostatic model used). Here, we use the simplest approach, where only the bulk–like viscous drag on the ions is taken into account, resulting in a mobility that is inversely proportional to the local viscosity.

In order to describe the dielectric profile at a similarly simplistic level as the viscosity, we use a step function as well,

$$\varepsilon_{\perp}(z) = \begin{cases} 1 & \text{if } z < z_{\perp}^{\mathrm{DDS}} \\ \varepsilon_{bulk} & \text{otherwise,} \end{cases} \tag{9}$$

with $z_{\perp}^{\mathrm{DDS}}$ the dielectric dividing surface as defined as [34]

$$z_{\perp}^{\mathrm{DDS}} = z_v + \int_{z_v}^{z_l} \frac{\varepsilon_{\perp}^{-1}(z_l) - \varepsilon_{\perp}^{-1}(z)}{\varepsilon_{\perp}^{-1}(z_l) - \varepsilon_{\perp}^{-1}(z_v)}\,\mathrm{d}z, \tag{10}$$

where z_v and z_l are positions in the solid and liquid phase, respectively. The profile in Eq. 9 is designed to reproduce the electrostatic potential calculated in molecular dynamics simulations at positions $z \gtrsim 1$ nm from the interface [34]. For $z_{\perp}^{\mathrm{DDS}}$ we use two different values: $z_{\perp}^{\mathrm{DDS}} = 0.10$ nm, corresponding to a hydrophilic surface, and $z_{\perp}^{\mathrm{DDS}} = 0.12$ nm, corresponding to a very hydrophobic surface, as directly taken from Ref. [34]. The inverse dielectric profiles $\varepsilon_{\perp}^{-1}(z)$ in the approximation of Eq. 9 are shown in Fig. 2 (b) for hydrophilic and very hydrophobic surfaces.

A simplified model where z_s and $z_{\perp}^{\mathrm{DDS}}$ are chosen equal will give qualitatively similar results. In the calculations below, however, we take the parameters z_s and $z_{\perp}^{\mathrm{DDS}}$ directly from molecular dynamics simulations. Doing so works very well for the dielectric dividing surface $z_{\perp}^{\mathrm{DDS}}$, as we will show on the basis of our results for the double–layer capacitance.

3 Scaling Analysis

In the following, we qualitatively investigate how the dielectric profile $\varepsilon_{\perp}(z)$ as given in Eq. 9 affects the counterion distribution, and consequently σ_{ek} and σ_c.

► **Counterions at a charged plate.** The electrokinetic and conductive surface charge densities defined in Eqs. 4 and 6 are directly affected by the viscosity profile $\eta(z)$. The dielectric profile $\varepsilon_{\perp}(z)$ does not affect σ_{ek} and σ_c directly, but it does have a decisive influence on the ion distribution, which in turn has a major impact on σ_{ek} and σ_c. For a qualitative picture of the effect of $\varepsilon_{\perp}(z)$, we consider the situation of an infinite charged plate in contact with a solution containing only counterions. We keep the viscosity constant, $\eta(z) = \eta_{bulk}$. According to the Gouy–Chapman model, the ions form a diffuse layer when $\varepsilon_{\perp}(z) = \varepsilon_{bulk}$, and by definition $\sigma_{ek} = \sigma_c = \sigma_0$. This relation is also valid in the limit of low salt concentration ($c_0 \to 0$), in which case the solution contains only counterions. Using the profile of Eq. 9, on the other hand, a large portion of the ions will condense into the low–dielectric area because of the steep increase of the electric potential resulting from the low dielectric constant. This model of a low–dielectric layer of condensed ions has been proposed long ago by Otto Stern based on experimental double layer capacitance data [42], and we have confirmed recently that Eq. 9 in conjunction with a mean–field model indeed reproduces the salt concentration dependence of the double layer capacitance [34]. In our present scaling analysis, we use a delta function as a model for the charge distribution to mimic the condensed layer of ions,

$$\rho(z) = -\sigma_0\delta(z - d), \tag{11}$$

with d the typical distance from the surface, which is treated in this scaling analysis as a parameter. The electro–osmotic mobility of Eq. 2 is integrated by parts, which leads to

$$\zeta = -\frac{1}{\varepsilon_0\varepsilon_{bulk}}\int_0^{\infty} z\,\rho(z)\,\mathrm{d}z, \tag{12}$$

using the definition of ζ given in Eq. 3. Inserting Eq. 11 into Eq. 12 gives

$$\zeta = \frac{\sigma_0\, d}{\varepsilon_0\varepsilon_{bulk}} \tag{13}$$

which scales linearly with σ_0 for a given distance d. The behavior of σ_{ek}, defined by Eq. 4 and using Eq. 13, as a function of σ_0 depends on how d behaves as a function of σ_0.

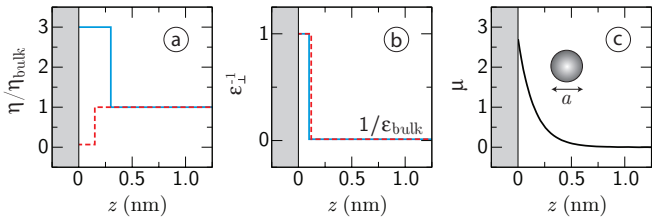

Figure 2: (a) Normalized viscosity profile (Eq. 7) at typical hydrophilic and hydrophobic surfaces (blue solid line and red dashed line respectively) and (b) Corresponding inverse dielectric profiles $\varepsilon_\perp^{-1}(z)$ (Eq. 9), showing a very small difference of 0.02 nm between the dielectric dividing surface positions at hydrophobic and hydrophilic surfaces. (c) Nonelectrostatic potential $\mu_\pm(z)$ (Eq. 22) with $\alpha = 1$. Also shown is an ion with diameter a.

To calculate the conductivity we insert Eq. 11 into Eq. 5,

$$\frac{I}{E_\parallel} = \int_0^\infty \left(-\sigma_0 \frac{u_\parallel(z)}{E_\parallel} + \nu|\sigma_0|\right) \delta(z-d)\, \mathrm{d}z, \qquad (14)$$

with ν being the electrophoretic mobility of the counterions. The flow at $z = d$ turns out to be $u_\parallel(d) = -E_\parallel \sigma_0 d/2\eta_{bulk}$, from which the conductivity follows as

$$\frac{I}{E_\parallel} = \frac{\sigma_0^2\, d}{2\eta_{bulk}} + \nu|\sigma_0|. \qquad (15)$$

Contrary to the electro–osmotic mobility, which depends linearly on σ_0, the conductivity scales with σ_0^2. That means that the conductive surface charge density σ_c will exceed the electrokinetic surface charge density σ_{ek} for large σ_0 (provided d does not become infinitesimally small), which rationalizes the experimentally measured excess surface conductivity that is sketched in Fig. 1 (c). The analysis above shows that the so–called *anomalous surface conduction* follows naturally from the standard dynamic equations when the double–layer width deviates from the standard mean–field prediction for a uniform dielectric constant.

4 The Modified Poisson–Boltzmann Equation

To quantitatively examine the electrokinetic and conductive surface charge densities σ_{ek} and σ_c as a function of the bare surface charge density σ_0, we solve the Poisson–Boltzmann equation in conjunction with the Stokes equation (Eq. 1) using the dielectric profile of Eq. 9 and the viscosity profile of Eq. 7.

We assume that the electric field is linearly related to the displacement field by the local inverse dielectric tensor $\varepsilon_\perp^{-1}(z)$,

$$\varepsilon_0 E_\perp(z) = \varepsilon_\perp^{-1}(z)\, D_\perp(z), \qquad (16)$$

where $\perp$ indicates the component perpendicular to the interface. Eq. 16 is a good approximation in case of a slowly varying $D_\perp(z)$ [34, 43]. Taking the derivative of Eq. 16 and using $\nabla\psi(z) = -E_\perp(z)$, with $\psi(z)$ the electrostatic potential, and $\nabla D_\perp(z) = \rho(z)$, with $\rho(z)$ the ionic charge density, we arrive at the modified Poisson equation

$$\varepsilon_0 \nabla^2\psi(z) = \varepsilon_\perp^{-1}(z)\,\rho(z) - D_\perp(z)\,\nabla\varepsilon_\perp^{-1}(z). \qquad (17)$$

The displacement field $D_\perp(z)$ is given by

$$D_\perp(z) = \int_0^z \rho(z')\,\mathrm{d}z'. \qquad (18)$$

Eqs. 17 and 18 constitute an integro–differential equation [44]. We consider a solution of monovalent ions. The free charge density is calculated from the ionic densities $c_+(z)$ and $c_-(z)$,

$$\rho(z) = e\,(c_+(z) - c_-(z)), \qquad (19)$$

with e the absolute charge of an electron. To ensure that the ionic density does not exceed its physical limit set by the ionic volume, we include a fermionic steric interaction to calculate the ionic densities from the unrestricted ionic densities $\tilde{c}_+(z)$ and $\tilde{c}_-(z)$ [32, 45, 46, 47, 48],

$$c_\pm(z) = \frac{\sqrt{2}\,\tilde{c}_\pm(z)}{\sqrt{2} + a_+^3\,(\tilde{c}_+(z) - c_0) + a_-^3\,(\tilde{c}_-(z) - c_0)}, \qquad (20)$$

with c_0 being the bulk salt concentration and a_+ and a_- being the diameters of positive and negative ions respectively. The denominator in Eq. 20 restricts the maximum density $c_\pm(z)$ to $\sqrt{2}\,a_\pm^{-3}$, which is the maximum density of close–packed (face–centered cubic or hexagonal close–packed) spheres of diameter $a_\pm$. The unrestricted ionic densities $\tilde{c}_+(z)$ and $\tilde{c}_-(z)$ follow the Boltzmann distribution

$$\tilde{c}_\pm(z) = c_0 \exp\left[-\mu_\pm(z) \mp \beta e \psi(z)\right], \qquad (21)$$

with β the inverse thermal energy and $\mu_+(z)$ and $\mu_-(z)$ the nonelectrostatic contribution to the potential of the positive and negative ions respectively. Combining Eqs. 17, 18, 19, 20 and 21 yields the modified Poisson–Boltzmann equation. It should be noted that the steric interaction of Eq. 20 becomes important only in case of high surface charge density, high salt concentration or large ion size [31]; its effect on the calculations presented here is minor.

► **Nonelectrostatic potential.** For the nonelectrostatic potential $\mu_\pm(z)$, we use a heuristic function of the form

$$\mu_\pm(z) = \alpha \exp\left[1 - 2z/a_\pm\right]. \qquad (22)$$

Beyond 1 nm away from the interface, the ionic potential of mean force – which includes dielectric as well as nonelectrostatic effects – typically shows a decreasing shape

that can be well approximated with the exponential form of Eq. 22 [49, 50]. Note, however, that different functional forms, such as a square–well potential, could be used equally well. The dependence of the nonelectrostatic potential on the surface and ion type is parameterized by the ion diameter $a_\pm$ and the interaction strength α. In Fig. 2 (c), we show the nonelectrostatic potential of Eq. 22 with $\alpha = 1$, together with a sketch of an ion with diameter a. In the following, we first set $\alpha = 0$ to show the trends of σ_{ek} and σ_c and then use α as a fit parameter to compare with experimental data.

► **Volume fraction.** Because it better reflects the distribution of the ions than the density of point charges, we plot the fraction $\varphi_\pm(z)$ of the volume occupied by ions, calculated by convolution of the point charge density with the molecular volume $v_\pm(z)$,

$$\varphi_\pm(z) = \int c_\pm(z')\, v_\pm(z - z')\, \mathrm{d}z', \tag{23}$$

with $v_\pm(z)\,\mathrm{d}z$ the volume of an ion slice of width $\mathrm{d}z$,

$$v_\pm(z) = \begin{cases} \pi\left(a_\pm^2/4 - z^2\right) & \text{if } |z| < a_\pm/2 \\ 0 & \text{otherwise.} \end{cases} \tag{24}$$

The volume fraction is used only for plotting the ion distribution; for all calculations we still assume that the charge is located at a single point in the center of the ion.

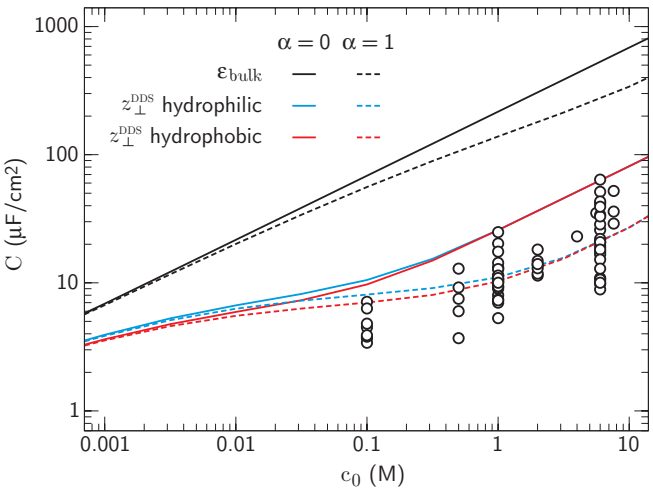

Figure 3: Double–layer capacitance $C = \mathrm{d}\sigma_0/\mathrm{d}\psi_0$, calculated from Eqs. 17–21 for two different approximations of the dielectric profile: $\varepsilon_\perp(z) = \varepsilon_{bulk}$ (black lines) and $\varepsilon_\perp(z)$ from Eq. 9, using $z_\perp^{\mathrm{DDS}} = 0.10$ nm (hydrophilic, blue lines) and $z_\perp^{\mathrm{DDS}} = 0.12$ nm (hydrophobic, red lines). Eq. 22 is used for the nonelectrostatic potential, with interaction strengths $\alpha = 0$ (solid lines) and $\alpha = 1$ (dashed lines). For the fermionic steric interaction we use $a_\pm = 0.3$ nm. Black circles represent experimental data on carbon-based surfaces in contact with aqueous electrolytes [34].

Table 1: Combinations of the width z_s and viscosity η_i of the interfacial layer used for the viscosity profile of Eq. 7.

Nº	Surface type	z_s (nm)	$\frac{\eta_{bulk}}{\eta_i}$	b (nm)[a]
1	Hydrophilic	0.3	1/3	−0.2
2	No slip	–	1	0.0
3	Moderately hydrophobic	0.15	5	0.6
4	Very hydrophobic	0.15	15	2.1

[a] The apparent slip length b according to Eq. 8.

5 Results and Discussion

We numerically solve the modified Poisson–Boltzmann equation (Eqs. 17–21) using a fixed bare surface charge density σ_0 located at $z = 0$ and vanishing electrostatic potential at infinity as boundary conditions. The ion centers are allowed to approach $z = 0$, thereby partly penetrating the solid, which accounts for surface softness. For the fermionic steric repulsion of Eq. 20 we use $a_\pm = 0.3$ nm.

► **Double–layer capacitance.** In Fig. 3, we show the double–layer capacitance $C = \mathrm{d}\sigma_0/\mathrm{d}\psi_0$, with ψ_0 being the potential at $z = 0$, as a function of the bulk salt concentration c_0, together with experimental results on different kinds of carbon–based surfaces [34]. Assuming $\varepsilon_\perp(z) = \varepsilon_{bulk}$ (black lines), the result of the Poisson–Boltzmann equation overestimates the experimental data by an order of magnitude. The experimental data is captured much better when the dielectric profile of Eq. 9 is used (red and blue lines). Quantitative agreement can be achieved when the repulsive nonelectrostatic potential $\mu_\pm(z)$ of Eq. 22 is taken into account in addition to the dielectric profile (red & blue dashed lines). The interaction strength needed to fit the data is of the order of unity; for the results in Fig. 3 we have used $\alpha = 1$. It has been known for nearly a century that the discrepancy between experimental capacitance data and the Gouy–Chapman model can be resolved by assuming a low–dielectric layer at the interface [42]. Fig. 3 shows that the modified Poisson–Boltzmann equation with the dielectric profile of Eq. 9, which indeed enhances the adsorption of ions into the low–dielectric region [36], provides an accurate description of the ion distribution, as well as the dielectric properties of the interfacial layer.

In Fig. 4 we show the volume fraction profile of counterions $\varphi_+(z)$, at bulk salt concentration $c_0 = 1$ mM, for two different approximations of the dielectric function: (a) $\varepsilon_\perp(z) = \varepsilon_{bulk}$ and (b) using $\varepsilon_\perp(z)$ from Eq.

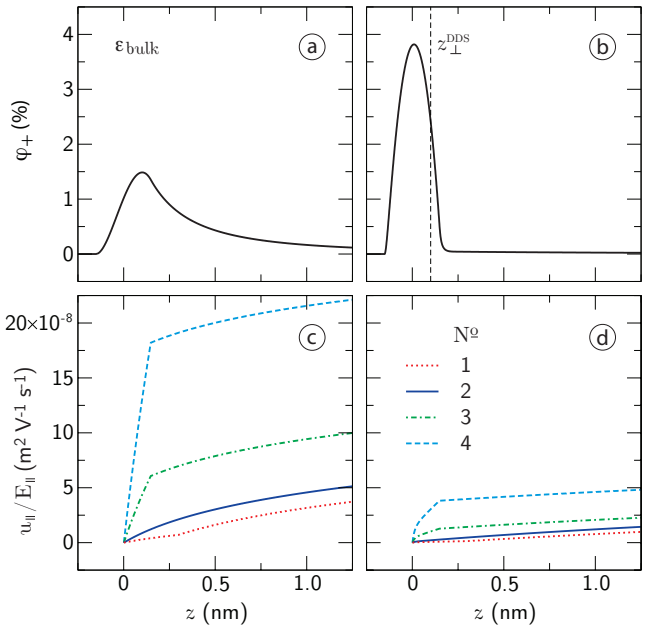

Figure 4: Volume fraction of ions, calculated from a convolution according to Eq. 23 of the ion density $c_+(z)$ with the molecular volume of Eq. 24, using (a) a bulk dielectric constant and (b) a dielectric dividing surface at $z_\perp^{\mathrm{DDS}} = 0.1$ nm, as appropriate for a hydrophilic surface. The corresponding electro–osmotic mobility is shown (c) for $\varepsilon_\perp(z) = \varepsilon_{bulk}$ and (d) for $\varepsilon_\perp(z)$ from Eq. 9, using four different viscosity profiles (Eq. 7 with the parameters listed in Tab. 1), with apparent slip length b calculated using Eq. 8: $\eta_{bulk}/\eta_i = 15$ and $z_s = 0.15$ nm ($b = 2.1$ nm, dashed lines), $\eta_{bulk}/\eta_i = 5$ and $z_s = 0.15$ nm ($b = 0.6$ nm, dash–dotted lines), no slip (solid lines) and $\eta_{bulk}/\eta_i = 1/3$ with $z_s = 0.3$ nm ($b = -0.2$ nm, dotted lines). The bare surface charge density equals $\sigma_0 = -0.6\ e/\mathrm{nm}^2$ and the bulk salt concentration is $c_0 = 1$ mM. For the steric interactions defined in Eq. 20 we use $a_+ = a_- = 0.3$ nm and no nonelectrostatic ion–wall interaction: $\mu_\pm(z) = 0$.

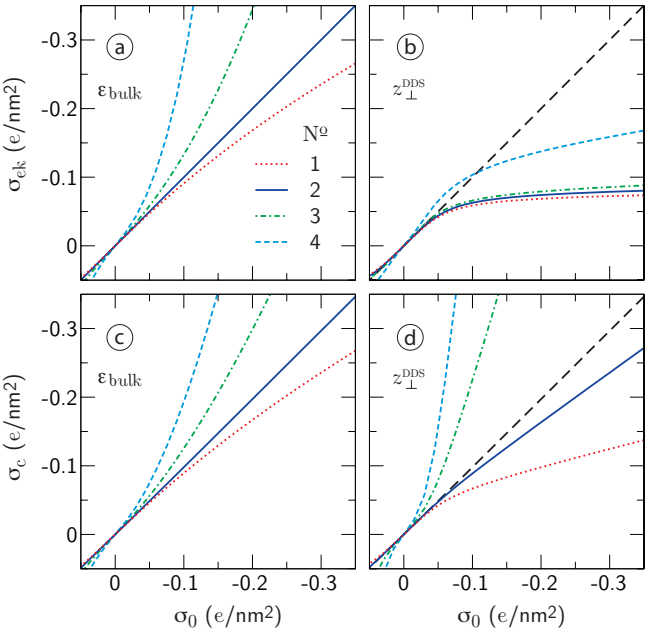

Figure 5: Electrokinetic surface charge density σ_{ek} (a, b) and conductive surface charge density σ_c (c, d) as a function of the bare surface charge density σ_0, using a bulk dielectric constant $\varepsilon_\perp(z) = \varepsilon_{bulk}$ on the left (a, c) and using $\varepsilon_\perp(z)$ from Eq. 9 on the right (b, d), with $z_\perp^{\mathrm{DDS}} = 0.1$ nm (hydrophilic) when $b \le 0$ and $z_\perp^{\mathrm{DDS}} = 0.12$ nm (hydrophobic) when $b > 0$. The parameters of the viscosity profiles used are listed in Tab. 1: Nº 1. hydrophilic, dotted lines ($z_s = 0.3$ nm, $\eta_{bulk}/\eta_i = 1/3$, $b = -0.2$ nm); Nº 2. no slip, solid lines ($\eta_i = \eta_{bulk}$, $b = 0$); Nº 3. moderately hydrophobic, dashed–dotted lines ($z_s = 0.15$ nm, $\eta_{bulk}/\eta_i = 5$, $b = 0.6$ nm); Nº 4. very hydrophobic, dashed lines ($z_s = 0.15$ nm, $\eta_{bulk}/\eta_i = 15$, $b = 2.1$ nm). For all curves, the bulk salt concentration is $c_0 = 1$ mM. No nonelectrostatic interaction potential is used, $\mu_\pm(z) = 0$, and steric interaction with $a_\pm = 0.3$ nm.

9 with the hydrophilic $z_\perp^{\mathrm{DDS}} = 0.1$ nm. The nonelectrostatic interaction is set to zero, $\mu_\pm(z) = 0$. The bare surface charge density is $\sigma_0 = -0.6\ e/\mathrm{nm}^2$, which is the value measured for silica at 10^{-3} M KCl and pH = 8 [1]. Clearly, the counterions accumulate much closer to the wall when the dielectric profile is taken into account, which is due to the steep increase of the potential in the low–dielectric region. It should be noted that, although the density of ions directly at the wall is enhanced, it never exceeds its physical limit because of the fermionic steric repulsion introduced in Eq. 20. The electro–osmotic mobility $u_\parallel(z)/E_\parallel$ in the first nanometer next to the surface, calculated from Eq. 2, is shown in Figs. 4 (c)–(d) using the viscosity profile from Eq. 7 with four different combinations of η_i and z_s, which are listed in Tab. 1. Each combination can be characterized by its apparent slip length using Eq. 8: very hydrophobic ($\eta_{bulk}/\eta_i = 15$ and $z_s = 0.15$ nm, giving $b = 2.1$ nm), moderately hydrophobic ($\eta_{bulk}/\eta_i = 5$ and $z_s = 0.15$ nm, giving $b = 0.6$ nm), no slip ($\eta_i = \eta_{bulk}$, $b = 0$) and hydrophilic ($\eta_{bulk}/\eta_i = 1/3$ and $z_s = 0.3$ nm, giving $b = -0.2$ nm). Figs. 4 (c) and (d) already show a strikingly different behavior: the mobility is significantly lower in Fig. 4 (d), where a dielectric dividing surface $z_\perp^{\mathrm{DDS}}$ is taken into account via Eq. 9, compared to Fig. 4 (c), where ε_{bulk} is used.

► **First puzzle: Saturation of σ_{ek}.** In Fig. 5, we plot (a) the electrokinetic surface charge density σ_{ek}, defined in Eq. 4, and (c) the conductive surface charge density σ_c, defined in Eq. 6 as a function of the bare surface charge density σ_0, using a bulk dielectric constant ($\varepsilon_\perp(z) = \varepsilon_{bulk}$) and four different viscosity profiles (Eq. 7 with the parameters listed in Tab. 1). Using the very hydrophobic viscosity profile (Nº 4. in Tab. 1, $b = 2.1$ nm) or the moderately hydrophobic profile (Nº 3. in Tab. 1, $b = 0.6$ nm), the electrokinetic surface charge density σ_{ek} exceeds the bare surface charge density σ_0, contrary to experimental evidence [18]. The correct behavior, $\sigma_{ek} < \sigma_0$, is only recovered when using a viscous

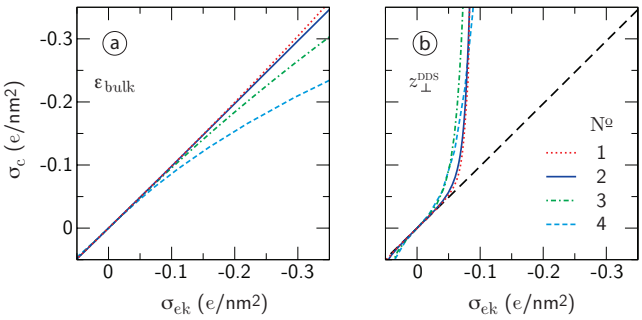

Figure 6: Conductive surface charge density σ_c versus electrokinetic surface charge density σ_{ek}, (a) using $\varepsilon_\perp(z) = \varepsilon_{bulk}$ and (b) using Eq. 9 with $z_\perp^{\mathrm{DDS}} = 0.1$ nm (hydrophilic) when $b \leq 0$ and $z_\perp^{\mathrm{DDS}} = 0.12$ nm (hydrophobic) when $b > 0$. Eq. 7 is used for the viscosity profile, with the parameters listed in Tab. 1. For all curves, the bulk salt concentration is $c_0 = 1$ mM. No nonelectrostatic interaction potential is used, $\mu_\pm(z) = 0$, while steric interaction (Eq. 20) is included with $a_\pm = 0.3$ nm.

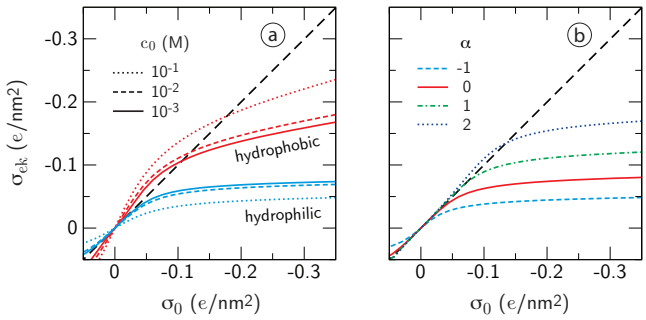

Figure 7: (a) Effect of the bulk salt concentration c_0 on the electrokinetic surface charge density σ_{ek} as a function of the bare surface charge density σ_0 for hydrophilic surfaces (blue lines), calculated using $z_s = 0.3$ and $\eta_{bulk}/\eta_i = 1/3$ (№ 1. in Tab. 1) in combination with $z_\perp^{\mathrm{DDS}} = 0.10$ nm, and for hydrophobic surfaces (red lines), calculated using $z_s = 0.15$ nm and $\eta_{bulk}/\eta_i = 15$ (№ 4. in Tab. 1) in combination with $z_\perp^{\mathrm{DDS}} = 0.12$ nm. For all curves $a_\pm = 0.3$ nm and $\mu_\pm(z) = 0$. (b) Dependence of σ_{ek} on the strength α of the nonelectrostatic potential $\mu_\pm(z)$ given in Eq. 22. For illustration purposes, we use the hydrophilic dielectric dividing surface $z_\perp^{\mathrm{DDS}} = 0.10$ nm and bulk viscosity $\eta_i = \eta_{bulk}$. The bulk salt concentration $c_0 = 1$ mM.

layer (№ 1. in Tab. 1, $b = -0.2$ nm). At the same time, however, σ_c is also lowered, at roughly the same rate as σ_{ek}, see Fig. 5 (c). When a dielectric dividing surface is introduced, shown in Figs. 5 (b) & (d), the electrokinetic surface charge density saturates as a function of the bare surface charge density for all viscosity profiles. Because experiments show that saturation of σ_{ek} occurs at every surface type, we conclude that a dielectric profile of the form of Eq. 9 is necessary to explain the trend of the experimental mobility data that is sketched in Fig. 1 (b). The main effect of the hydrodynamic boundary condition is that σ_{ek} saturates at higher values at hydrophobic surfaces then at hydrophilic ones, again in agreement with experimental data [51]. Interestingly, the electrokinetic surface charge density of the very hydrophobic surface rises above σ_0 for low values of σ_0, to which we will come back below.

► **Second puzzle: Anomalous surface conductivity.** We plot the conductive surface charge density σ_c as a function of the electrokinetic surface charge density σ_{ek} in Fig. 6, using (a) $\varepsilon_\perp(z) = \varepsilon_{bulk}$ and (b) the dielectric profile of Eq. 9. Without dielectric profile, σ_c is close to, or below σ_{ek}, whereas σ_c features a steep increase when the dielectric profile is used, in agreement with the experimental trends sketched in Fig. 1 (c). Thus the excess conductivity, which is traditionally referred to as anomalous surface conductance [52, 26, 24, 25], follows directly from the dielectric profile $\varepsilon_\perp(z)$.

► **Third puzzle: Salt–concentration dependence of σ_{ek}.** In Fig. 7 (a), we plot the electrokinetic surface charge density σ_{ek} as a function of the bare surface charge density σ_0 at different values of the bulk salt concentration c_0. Curves are shown for a very hydrophobic surface (№ 4. in Tab. 1: $b = 2.1$ nm and $z_\perp^{\mathrm{DDS}} = 0.12$ nm) and for a typical hydrophilic surface (№ 1. in Tab. 1: $b = -0.2$ nm and $z_\perp^{\mathrm{DDS}} = 0.10$ nm). Clearly, the electrokinetic surface charge density is higher at hydrophobic surfaces than at hydrophilic surfaces at all salt concentrations, in accordance with experimental results [51, 18]. The difference between the surface types is primarily caused by the different viscosity profiles; $z_\perp^{\mathrm{DDS}}$ is comparable for both surface types. Similar to the experimental trend sketched in Fig. 1 (d) [18], the behavior as a function of salt concentration is opposite at the two surface types: Whereas σ_{ek} increases with increasing salt concentration at the hydrophobic surface, it decreases with increasing salt concentration at the hydrophilic surface. The reason for this opposite behavior is that for moderate and high bulk salt concentration, $c_0 > 10^{-3}$ M, the charge distribution shifts towards the wall upon increasing c_0 (decreasing Debye screening length), and more charge is located in the region of varying viscosity. At hydrophilic surfaces, the effect of the higher viscosity in the interfacial layer is to decrease the electrokinetic surface charge density σ_{ek}, whereas at hydrophobic surfaces the low viscosity increases σ_{ek}. At low salt concentrations, $c_0 \leq 10^{-3}$ M, the effect diminishes because the charge within the interfacial layer goes to zero, and therefore becomes irrelevant.

Apart from the dependence on surface type discussed above, the electrokinetic surface charge density also depends on the specific ion–surface interaction, which has a significant nonelectrostatic component. In our calculations, this contribution is modeled by the function $\mu_\pm(z)$ given in Eq. 22, which has only one parameter, the interaction strength α (keeping the decay length fixed and equal to the ion diameter $a_\pm$). In Fig. 7 (b), we plot σ_{ek} as a function of σ_0 for different values of the non-

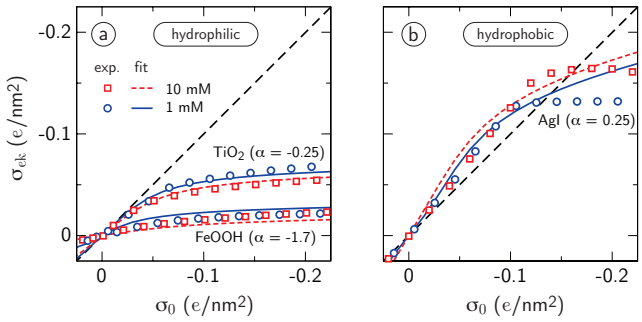

Figure 8: Comparison of theory predictions to experimental data from Ref. [18] (symbols), taken at different concentrations KNO_3. Data points do not correspond to individual measurements – they are merely a discretization of the curves presented in Ref. [18]. In order to cancel the surface conduction correction [18], the hydrophilic curves have been reconstructed according to $\sigma_{ek} = \sinh\left(\sinh^{-1}\left(\sigma_{ek}^{corr.}\right)/1.55\right)$, with $\sigma_{ek}^{corr.}$ the values reported in Ref. [18]. For the hydrophilic curves, $z_\perp^{\mathrm{DDS}} = 0.10$ nm, $z_s = 0.3$ nm and $\eta_i = 3\eta_{bulk}$, giving $b = -0.2$ nm (viscosity profile Nº 1 in Tab. 1). For the hydrophobic curves, $z_\perp^{\mathrm{DDS}} = 0.12$ nm, $z_s = 0.15$ nm and $\eta_i = \eta_{bulk}/15$, giving $b = 2.1$ nm (viscosity profile Nº 4 in Tab. 1).

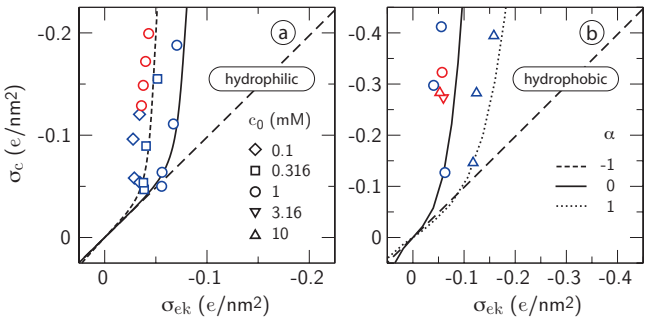

Figure 9: Conductive surface charge density σ_c versus electrokinetic surface charge density σ_{ek} for different systems in contact with a KCl solution of bulk concentration c_0. (a) Data from rectangular silica channels (dark blue, Ref. [21]) and monodisperse porous silica particles (red, Ref. [53]). (b) Data from monodisperse spherical polystyrene particles (dark blue, Ref. [26] and red, Ref. [54]). Curves are shown for interaction parameters $\alpha = 0$ and $\alpha = -1$ (hydrophilic) and $\alpha = 0$ and $\alpha = 1$ (hydrophobic), using a bulk concentration of 1 mM.

electrostatic interaction strength α for fixed $c_0 = 1$ mM. Positive values of α repel ions from the surface, thereby increasing σ_{ek}, whereas negative values attract ions to the surface, decreasing σ_{ek}. Interestingly, varying α within a moderate range of only several times the thermal energy has an equally large effect on σ_{ek} as the surface–type dependence shown in Fig. 7 (a). To determine realistic values of α, the surface adsorption excess could be compared with molecular dynamics simulations. Simulations of uncharged polar and nonpolar self–assembled monolayers show that ions are attracted to polar surfaces, but repelled from nonpolar ones [50]. From these results we expect that α is negative for hydrophilic surfaces and positive for hydrophobic surfaces. Note that the ion–surface potential may be much more complex than the simple form assumed in Eq. 22, but for the present purpose a generic exponential potential is sufficient.

6 Fitting Experimental Data

In the previous sections we have shown that the dielectric profile of Eq. 9 induces condensation of ions into a thin layer, and that the resulting electrokinetic and conductive surface charge densities qualitatively reproduce the experimental trends sketched in Fig. 1. In the following, we fit the model to published experimental data using the interaction strength α of the nonelectrostatic potential $\mu_\pm(z)$, given in Eq. 22, as a free parameter.

In Fig. 8, we show measurements of the electrokinetic surface charge density σ_{ek} taken from Ref. [18] as symbols, together with the fitted results of our model. At the hydrophilic surfaces, in Fig. 8 (a), the model captures the data very well over the entire range of the bare surface charge density σ_0. Note that the data presented in Ref. [18] have been corrected using a different model for the anomalous surface conduction, and that the raw data reproduced here have been reconstructed. At the hydrophobic surface, in Fig. 8 (b) the electrokinetic surface charge density exceeds the bare surface charge density for $|\sigma_0| < 0.15\ e/\mathrm{nm}^2$, which is reproduced by the model. Originally, this apparent excess electrokinetic mobility was considered to be a measurement error [18]. From our calculations we conclude, however, that it is possibly caused by hydrodynamic slip at the hydrophobic solid surface. At high absolute values of the bare surface charge density σ_0, the model disagrees with the experimental data at the hydrophobic surface, which probably has to do with the simplified model used. The fit parameter α is negative at the hydrophilic surfaces, indicating that ions are attracted to polar surfaces, and slightly positive at the hydrophobic surface, indicating that ions are repelled from nonpolar surfaces, in line with results from molecular dynamics simulations [50]. Again, the opposite trend of σ_{ek} as a function of bulk salt concentration at the two surface types in Fig. 8 is captured very well within our model.

As symbols in Fig. 9, we reproduce experimental data of the conductive surface charge density σ_c as a function of the electrokinetic surface charge density σ_{ek} at (a) hydrophilic surfaces and (b) hydrophobic surfaces in contact with a KCl solution at several low salt concentrations c_0. The data on silica particles [53] and polystyrene particles [26, 54] have been taken from literature directly. The data on rectangular silica channels [21] have been fitted numerically with the Gouy–Chapman model for a slit–like geometry to extract σ_{ek} and σ_c from the streaming potential and the electrical conductance, respectively.

The spread in the data is likely to be caused by the different materials and geometries used in the experiments. In Fig. 9 (a), we show results from our model for the hydrophilic viscosity profile (№ 1. in Tab. 1: $b = -0.2$ nm) using $\alpha = 0$ (solid line) and $\alpha = -1$ (broken line) for illustration. The salt concentration for the calculated curves is $c_0 = 1$ mM, because at low salt concentration the dependence of σ_{ek} and σ_c on c_0 is minor. The model captures the data very well, using an attractive nonelectrostatic potential with an interaction strength between $\alpha = 0$ and $\alpha \simeq -1$. For the curves in Fig. 9 (b), we use the viscosity profile № 4. in Tab. 1 ($b = 2.1$ nm), as appropriate for very hydrophobic surfaces. We use $\alpha = 0$ (solid line) and $\alpha = 1$ (dotted line), showing that the hydrophobic surface can be modeled with a nonelectrostatic interaction around $\alpha = 0$, or a slightly repulsive potential of the order of $\alpha = 1$. The slight nonelectrostatic attraction at the hydrophilic surface and repulsion at the hydrophobic surface corresponds well to the fit parameters used to model σ_{ek} in Fig. 8, as well as to the trend expected from simulations of uncharged polar and nonpolar surfaces [50]. However, fitting the capacitance data shown in Fig. 3, which is taken in a different concentration regime, requires a repulsive nonelectrostatic potential for all data. The only difference in the model is the use of the viscosity profile for the comparison in Figs. 8 and 9, which is not needed to calculate the capacitance in Fig. 3. Therefore, the discrepancy is likely to be related fact that we use the viscosity profiles from molecular dynamics simulations at atomically smooth surfaces. A more accurate viscosity profile, or including the effect of surface roughness, may reconciliate the different results.

7 Conclusions

Using a dielectric profile with a low–dielectric layer at the interface, as extracted from molecular dynamics simulations, in a modified Poisson–Boltzmann equation we are able to explain three well–established experimental puzzles that have not been understood within the context of a single model before. First, we capture the saturation of the electro–osmotic surface charge density σ_{ek} as a function of the bare surface charge density. Second, we explain the excess surface conductivity commonly measured in electrokinetic experiments, making the assumption of anomalous electrical conductance behind the shear plane superfluous. Third, we reproduce the opposite trend of the electro–osmotic mobility as a function of salt concentration at hydrophilic and hydrophobic surfaces. The physical mechanism leading to the observed behavior is the enhanced condensation of ions close to the surface, which is due to the low effective dielectric constant of interfacial water. This causes saturation of the electrokinetic surface charge density, but not of the conductive surface charge density, explaining the notion of anomalous excess surface conductivity.

We have left out a number of important effects from our modeling, for example, charge regulation at the surface as a function of varying salt concentration, surface roughness and curvature, electrofriction effects [55], as well as electrostatic correlation effects beyond the mean–field level [56]. We have also modeled the viscosity and dielectric profiles by simple square–well functions and the nonelectrostatic surface–ion interaction by an exponentially decaying function. At the current stage, our model seems to contain sufficient complexity to explain a number of at–first–sight disconnected and hitherto puzzling experimental findings and trends. Needless to say, however, it only constitutes a first step in efforts to describe the electrostatics and electrokinetics of charged surfaces in a unified framework.

► **Acknowlegments.** We thank the Deutsche Forschungsgemeinschaft for funding via Nanosystems Initiative Munich.

Appendix

We derive the electro–osmotic mobility, the electrokinetic surface charge density and the conductive surface charge density from the Gouy–Chapman model.

► **Gouy–Chapman model.** The standard Poisson equation is given by

$$\varepsilon_0 \varepsilon_{bulk} \nabla^2 \psi(z) = -\rho(z). \tag{25}$$

According to the standard Boltzmann equation, the charge density $\rho(z)$ equals

$$\rho(z) = -2ec_0 \sinh[\beta e \psi(z)]. \tag{26}$$

The solution to the Poisson–Boltzmann equation (Eqs. 25–26) for a monovalent electrolyte at a charged plane is

$$\psi(z) = -\frac{2}{\beta e} \ln \frac{1 + \gamma \exp[-\kappa z]}{1 - \gamma \exp[-\kappa z]}, \tag{27}$$

with

$$\gamma = -\kappa\lambda + \sqrt{\kappa^2\lambda^2 + 1}. \tag{28}$$

The inverse Debye screening length κ and the Gouy–Chapman length λ are given by

$$\kappa = \sqrt{\frac{2e^2 c_0 \beta}{\varepsilon_0 \varepsilon_{bulk}}} \quad \text{and} \quad \lambda = \frac{2\varepsilon_0 \varepsilon_{bulk}}{\beta e |\sigma|}. \tag{29}$$

The electro–osmotic mobility is related to the charge density by the Stokes equation, which reads

$$\eta_{bulk} \nabla^2 u_{\parallel}(z) = -\rho(z) E_{\parallel}, \tag{30}$$

for spatially constant viscosity η_{bulk}.

► **Electro–osmotic mobility.** Eliminating the charge density $\rho(z)$ from Eqs. 25 and 30 yields

$$\varepsilon_0 \varepsilon_{bulk} \nabla^2 \psi(z) = \frac{\eta_{bulk}}{E_{\parallel}} \nabla^2 u_{\parallel}(z). \tag{31}$$

Integrating twice with boundary conditions $\nabla\psi(z) = \nabla u_{\parallel}(z) = 0$ for $z \to \infty$ and the no–slip boundary condition $u_{\parallel}(0) = 0$ gives the electro–osmotic mobility,

$$\frac{u_{\parallel}(z)}{E_{\parallel}} = \frac{\varepsilon_0 \varepsilon_{bulk}}{\eta_{bulk}} \left[\psi(z) - \psi(0)\right]. \tag{32}$$

Defining $\psi(0) = \zeta$ and using $\psi(z \to \infty) = 0$ leads to the Helmholtz–Smoluchowski equation as shown in Eq. 3.

► **Electrokinetic surface charge density.** To solve the Poisson–Boltzmann equation (given by Eqs. 25 and 26) for a fixed surface charge density σ, we multiply both sides of Eqs. 25 and 26 by $2\nabla\psi(z)$, giving

$$\varepsilon_0 \varepsilon_{bulk} \nabla \left[\nabla\psi(z)\right]^2 = 4ec_0 \sinh\left[\beta e\psi(z)\right] \nabla\psi(z). \tag{33}$$

Integrating both sides, we arrive at

$$\varepsilon_0 \varepsilon_{bulk} \left[\nabla\psi(z)\right]^2 = \frac{4c_0}{\beta} \left(\cosh\left[\beta e\psi(z)\right] - 1\right), \tag{34}$$

where we used $\cosh\left[\beta e\psi(z)\right] = 1$ for $\psi(z) = 0$. Rewriting with the help of $\sqrt{\cosh x - 1} = \sqrt{2}\sinh\left[x/2\right]$, we arrive at

$$\nabla\psi(z) = -\sqrt{\frac{8c_0}{\beta\varepsilon_0\varepsilon_{bulk}}} \sinh\left[\frac{\beta e\psi(z)}{2}\right], \tag{35}$$

where the minus sign applies because $\nabla\psi(z)$ must be negative for positive values of $\psi(z)$. From the electroneutrality condition and $\nabla\psi(z) = 0$ for $z \to \infty$ we find that the surface charge density equals

$$\sigma = -\int_0^{\infty} \rho(z)\,\mathrm{d}z = -\varepsilon_0\varepsilon_{bulk}\nabla\psi(0). \tag{36}$$

Combining Eq. 35 with Eq. 36 gives the Grahame equation

$$\sigma = \sqrt{\frac{8c_0\varepsilon_0\varepsilon_{bulk}}{\beta}} \sinh\left[\frac{\beta e\,\psi(0)}{2}\right]. \tag{37}$$

Eq. 37 defines the electrokinetic surface charge density σ_{ek} when for $\psi(0)$ the ζ–potential of Eq. 3 is used.

► **Conductive surface charge density.** The surface conductivity is given by Eq. 5. Similar to the Grahame equation, the surface conductivity can be expressed as an equivalent surface charge density using the Gouy–Chapman theory. For convenience, we split Eq. 5 in three parts: the convective part (first line),

$$\frac{I^{(1)}}{E_{\parallel}} = \int_0^{\infty} e\left[c_+(z) - c_-(z)\right]\left[u_{\parallel}(z)/E_{\parallel}\right]\mathrm{d}z, \tag{38}$$

and two conductive parts (second line),

$$\begin{aligned} \frac{I^{(2)}}{E_{\parallel}} &= \int_0^{\infty} e\nu_+\left(c_+(z) - c_0\right)\mathrm{d}z \\ \frac{I^{(3)}}{E_{\parallel}} &= \int_0^{\infty} e\nu_-\left(c_-(z) - c_0\right)\mathrm{d}z. \end{aligned} \tag{39}$$

Inserting the electro–osmotic mobility of Eq. 32 and the charge density of Eq. 25 in Eq. 38 gives

$$\frac{I^{(1)}}{E_{\parallel}} = -\frac{\varepsilon_0^2\varepsilon_{bulk}^2}{\eta_{bulk}} \int_0^{\infty} \nabla^2\psi(z)\left[\psi(z) - \psi(0)\right]\mathrm{d}z, \tag{40}$$

which can be integrated by parts to give

$$\frac{I^{(1)}}{E_{\parallel}} = \frac{\varepsilon_0^2\varepsilon_{bulk}^2}{\eta_{bulk}} \int_0^{\infty} \left[\nabla\psi(z)\right]^2\mathrm{d}z, \tag{41}$$

using $\nabla\psi(z) = 0$ for $z \to \infty$. Inserting the derivative of Eq. 27 in Eq. 41 yields

$$\begin{aligned} \frac{I^{(1)}}{E_{\parallel}} &= \frac{\varepsilon_0^2\varepsilon_{bulk}^2}{\eta_{bulk}} \int_0^{\infty} \left[\frac{4\kappa\gamma\exp\left[-\kappa z\right]}{\beta e\left(1 - \gamma^2\exp\left[-2\kappa z\right]\right)}\right]^2 \mathrm{d}z \\ &= \frac{\varepsilon_0^2\varepsilon_{bulk}^2}{\eta_{bulk}} \left[-\frac{8\kappa\gamma^2\exp\left[-2\kappa z\right]}{\beta^2 e^2\left(1 - \gamma^2\exp\left[-2\kappa z\right]\right)}\right]_0^{\infty} \\ &= \frac{\varepsilon_0^2\varepsilon_{bulk}^2}{\eta_{bulk}} \frac{8\kappa\gamma^2}{\beta^2 e^2\left(1 - \gamma^2\right)}. \end{aligned} \tag{42}$$

The second part of the conductivity equals

$$\begin{aligned} \frac{I^{(2)}}{E_{\parallel}} &= \int_0^{\infty} e\nu_+ c_0 \left[\left(\frac{1 + \gamma\exp\left[-\kappa z\right]}{1 - \gamma\exp\left[-\kappa z\right]}\right)^2 - 1\right]\mathrm{d}z \\ &= \int_0^{\infty} e\nu_+ c_0 \left[\frac{4\gamma\exp\left[-\kappa z\right]}{\left(1 - \gamma\exp\left[-\kappa z\right]\right)^2}\right]\mathrm{d}z \\ &= e\nu_+ c_0 \left[-\frac{4\gamma\exp\left[-\kappa z\right]}{\kappa\left(1 - \gamma\exp\left[-\kappa z\right]\right)}\right]_0^{\infty} \\ &= e\nu_+ c_0 \frac{4\gamma}{\kappa\left(1 - \gamma\right)}. \end{aligned} \tag{43}$$

Similarly,

$$\frac{I^{(3)}}{E_{\parallel}} = -e\nu_- c_0 \frac{4\gamma}{\kappa\left(1 + \gamma\right)}. \tag{44}$$

Summing up $I = \sum_i I^{(i)}$ and rewriting in terms of κ gives the total excess conductivity

$$\frac{I}{E_{\parallel}} = \frac{32\gamma^2 e^2 c_0^2}{\kappa^3\left(1 - \gamma^2\right)\eta_{bulk}} + \frac{4\gamma e c_0 \nu_+}{\kappa\left(1 + \gamma\right)} - \frac{4\gamma e c_0 \nu_-}{\kappa\left(1 - \gamma\right)}. \tag{45}$$

For simplicity, we assume $\nu_+ = \nu_- = \nu$, so Eq. 45 becomes

$$\frac{I}{E_{\parallel}} = \frac{\gamma^2}{1 - \gamma^2}\left[\frac{32e^2c_0^2}{\kappa^3\eta_{bulk}} + \frac{8ec_0\nu}{\kappa}\right], \tag{46}$$

which is inverted to give the following surface charge density, using Eqs. 28 and 29

$$\sigma = \frac{\kappa^2\eta_{bulk}}{4ec_0 + \nu\kappa^2\eta_{bulk}} \sqrt{\frac{I}{E_{\parallel}}} \sqrt{\frac{I}{E_{\parallel}} + \frac{32e^2c_0^2}{\kappa^3\eta_{bulk}} + \frac{8ec_0\nu}{\kappa}}. \tag{47}$$

Eq. 47 defines the conductive surface charge density σ_c when the conductivity is calculated using Eq. 5.

References

[1] Tadros, T. F. & Lyklema, J. Adsorption of potential-determining ions at the silica-aqueous electrolyte interface and the role of some cations. *J. Electroanal. Chem.* **17**, 267 (1968).

[2] Gonzenbach, U. T. *et al.* Tailoring the microstructure of particle-stabilized wet foams. *Langmuir* **23**, 1025 (2007).

[3] Lyklema, J. *Fundamentals of Interface and Colloid Science* (Academic Press, London, 1995).

[4] Hansen, J. & Löwen, H. Effective interactions between electric double layers. *Annu. Rev. Phys. Chem.* **51**, 209 (2000).

[5] Quemada, D. & Berli, C. Energy of interaction in colloids and its implications in rheological modeling. *Adv. Colloid Interface Sci.* **98**, 51 (2002).

[6] Tiselius, A. A new apparatus for electrophoretic analysis of colloidal mixtures. *Trans. Faraday Soc.* **33**, 524 (1937).

[7] Stone, H. A., Stroock, A. D. & Ajdari, A. Engineering flows in small devices: Microfluidics toward a lab-on-a-chip. *Annu. Rev. Fluid Mech.* **36**, 381 (2004).

[8] Squires, T. M. & Quake, S. R. Microfluidics: Fluid physics at the nanoliter scale. *Rev. Mod. Phys.* **77**, 977 (2005).

[9] Varotsos, P. A., Sarlis, N. V. & Skordas, E. S. Electric fields that "arrive" before the time derivative of the magnetic field prior to major earthquakes. *Phys. Rev. Lett.* **91**, 148501 (2003).

[10] Glover, P. W. J. & Jackson, M. D. Borehole electrokinetics. *The Leading Edge* **29**, 724 (2010).

[11] Hidalgo-Álvarez, R. *et al.* Electrokinetic properties, colloidal stability and aggregation kinetics of polymer colloids. *Adv. Colloid Interface Sci.* **67**, 1 (1996).

[12] Verwey, E. J. W. The electrical double layer and the stability of lyophobic colloids. *Chem. Rev.* **16**, 363 (1935).

[13] Bikerman, J. J. Ionic theory of electroosmosis, the current flow and the surface conductivity. *Z. Phys. Chem. A* **163**, 378 (1933).

[14] Bikerman, J. J. Die Oberflächenleitfähigkeit und ihre Bedeutung. *Kolloid Zeitschrift* **72**, 100 (1935).

[15] Lyklema, J. Surface conduction. *J. Phys.: Condens. Matter* **13**, 5027 (2001).

[16] Stein, D., Kruithof, M. & Dekker, C. Surface-charge-governed ion transport in nanofluidic channels. *Phys. Rev. Lett.* **93**, 035901 (2004).

[17] Van der Heyden, F. H. J., Stein, D. & Dekker, C. Streaming currents in a single nanofluidic channel. *Phys. Rev. Lett.* **95**, 116104 (2005).

[18] Lyklema, J. On the slip process in electrokinetics. *Colloids Surf. A* **92**, 41 (1994).

[19] Lyklema, J. & Overbeek, J. T. G. On the interpretation of electrokinetic potentials. *J. Colloid Sci.* **16**, 501 (1961).

[20] Barrat, J. & Bocquet, L. Large slip effect at a nonwetting fluid-solid interface. *Phys. Rev. Lett.* **82**, 4671 (1999).

[21] Van der Heyden, F. H. J., Bonthuis, D. J., Stein, D., Meyer, C. & Dekker, C. Power generation by pressure-driven transport of ions in nanofluidic channels. *Nanolett.* **7**, 1022 (2007).

[22] Van der Put, A. G. & Bijsterbosch, B. H. Electrokinetic measurements on concentrated polystyrene dispersions and their theoretical interpretation. *J. Colloid Interface Sci.* **92**, 499 (1982).

[23] O'Brien, R. W. & Perrins, W. T. The electrical conductivity of a porous plug. *J. Colloid Interface Sci.* **99**, 20 (1984).

[24] Zukoski, C. F. & Saville, D. A. The interpretation of electrokinetic measurements using a dynamic model of the Stern layer: I. the dynamic model. *J. Colloid Interface Sci.* **114**, 32 (1986).

[25] Zukoski, C. F. & Saville, D. A. The interpretation of electrokinetic measurements using a dynamic model of the Stern layer: II. Comparisons between theory and experiment. *J. Colloid Interface Sci.* **114**, 45 (1986).

[26] Van der Put, A. G. & Bijsterbosch, B. H. Electrokinetic measurements on concentrated polystyrene dispersions and their theoretical interpretation. *J. Colloid Interface Sci.* **92**, 499 (1983).

[27] Dukhin, S. S. Nonequilibrium electric surface phenomena. *Adv. Colloid Interface Sci.* **44**, 1 (1993).

[28] Lyklema, J. & Minor, M. On surface conduction and its role in electrokinetics. *Colloids Surf. A* **140**, 33 (1998).

[29] Hunter, R. J. The significance of stagnant layer conduction in electrokinetics. *Adv. Colloid Interface Sci.* **100**, 153 (2003).

[30] Hunter, R. J. *Foundations of Colloid Science* (Oxford University Press, Great Clarendon Street, Oxford, UK, 2001).

[31] Bazant, M. Z., Kilic, M. S., Storey, B. D. & Ajdari, A. Towards an understanding of induced-charge electrokinetics at large applied voltages in concentrated solutions. *Adv. Colloid Interface Sci.* **152**, 48 (2009).

[32] Bikerman, J. J. Structure and capacity of electrical double layer. *Philos. Mag.* **33**, 384 (1942).

[33] Grahame, D. C. Effects of dielectric saturation upon the diffuse double layer and the free energy of hydration of ions. *J. Chem. Phys.* **18**, 903 (1950).

[34] Bonthuis, D. J., Gekle, S. & Netz, R. R. Dielectric profile of interfacial water and its effect on double-layer capacitance. *Phys. Rev. Lett.* **107**, 166102 (2011).

[35] Sendner, C. *et al.* Interfacial water at hydrophobic and hydrophilic surfaces: Slip, viscosity, and diffusion. *Langmuir* **25**, 10768 (2009).

[36] Bonthuis, D. J., Gekle, S. & Netz, R. R. Profile of the static permittivity tensor of water at interfaces: Consequences for capacitance, hydration interaction and ion adsorption. *Langmuir* **28**, 7679 (2012).

[37] Guo, X., Kirton, G. F. & Dubin, P. L. Carboxylated ficolls: Preparation, characterization, and electrophoretic behavior of model charged nanospheres. *J. Phys. Chem. B* **110**, 20815 (2006).

[38] Bonthuis, D. J. *et al.* Electrokinetics at aqueous interfaces without mobile charges. *Langmuir* **26**, 12614 (2010).

[39] Joly, L., Ybert, C., Trizac, E. & Bocquet, L. Hydrodynamics within the electric double layer on slipping surfaces. *Phys. Rev. Lett.* **93**, 257805 (2004).

[40] Wu, P. & Qiao, R. Physical origins of apparently enhanced viscosity of interfacial fluids in electrokinetic transport. *Phys. Fluids* **23**, 072005 (2011).

[41] Jouyban, A. & Kenndler, E. Theoretical and empirical approaches to express the mobility of small ions in capillary electrophoresis. *Electrophoresis* **27**, 992 (2006).

[42] Stern, O. Zur Theorie der electrolytischen Doppelschicht. *Z. Elektrochem.* **30**, 508 (1924).

[43] Kornyshev, A. A., Schmickler, W. & Vorotyntsev, M. A. Nonlocal electrostatic approach to the problem of a double layer at a metal-electrolyte interface. *Phys. Rev. B* **25**, 5244 (1982).

[44] Paillusson, F. & Blossey, R. Slits, plates, and Poisson-Boltzmann theory in a local formulation of nonlocal electrostatics. *Phys. Rev. E* **82**, 052501 (2010).

[45] Eigen, M. & Wicke, E. The thermodynamics of electrolytes at higher concentration. *J. Phys. Chem.* **58**, 702 (1954).

[46] Kralj-Iglič, V. & Iglič, A. Influence of finite size of ions on elecrostatic properties of electric double layer. *Electrotechnical Review (Ljubljana, Slovenija)* **61**, 127 (1994).

[47] Borukhov, I., Andelman, D. & Orland, H. Steric effects in electrolytes: A modified Poisson-Boltzmann equation. *Phys. Rev. Lett.* **79**, 435 (1997).

[48] Borukhov, I., Andelman, D. & Orland, H. Adsorption of large ions from an electrolyte solution: a modified Poisson-Boltzmann equation. *Electrochim. Acta* **46**, 221 (2000).

[49] Horinek, D. *et al.* Molecular hydrophobic attraction and ion-specific effects studied by molecular dynamics. *Langmuir* **24**, 1271 (2008).

[50] Schwierz, N., Horinek, D. & Netz, R. R. Reversed anionic Hofmeister series: The interplay of surface charge and surface polarity. *Langmuir* **26**, 7370 (2010).

[51] Churaev, N. V., Ralston, J., Sergeeva, I. P. & Sobolev, V. D. Electrokinetic properties of methylated quartz capillaries. *Adv. Colloid Interface Sci.* **96**, 265 (2002).

[52] Van der Put, A. G. & Bijsterbosch, B. H. Electrical conductivity of dilute and concentrated aqueous dispersions of monodisperse polystyrene particles. influence of surface conductance and double-layer polarization. *J. Colloid Interface Sci.* **75**, 512 (1980).

[53] Löbbus, M., Sonnfeld, J., Van Leeuwen, H. P., Volgelsberger, W. & Lyklema, J. An improved method for calculating zeta-potentials from measurements of the electrokinetic sonic amplitude. *J. Colloid Interface Sci.* **229**, 174 (2000).

[54] Minor, M., Van der Linde, A. J. & Lyklema, J. Streaming potentials and conductivities of latex plugs in indifferent electrolytes. *J. Colloid Interface Sci.* **203**, 177 (1998).

[55] Kim, Y.-W. & Netz, R. R. Electro-osmosis at inhomogeneous charged surfaces: Hydrodynamic versus electric friction. *J. Chem. Phys.* **124**, 114709 (2006).

[56] Boroudjerdi, H. *et al.* Statics and dynamics of strongly charged soft matter. *Phys. Rep.* **416**, 129 (2005).